International Journal of Remote Sensing

ISSN: 0143-1161 (Print) 1366-5901 (Online) Journal homepage: www.tandfonline.com/journals/tres20

Assessing optical water types in Asian coastal ocean waters from space using GCOM-C/SGLI observations

Eko Siswanto

To cite this article: Eko Siswanto (2025) Assessing optical water types in Asian coastal ocean waters from space using GCOM-C/SGLI observations, International Journal of Remote Sensing, 46:6, 2337-2357, DOI: 10.1080/01431161.2025.2450567

To link to this article: https://doi.org/10.1080/01431161.2025.2450567

Published online: 15 Jan 2025.

INTERNATIONAL JOURNAL OF REMOTE SENSING
2025, VOL. 46, NO. 6, 2337–2357
https://doi.org/10.1080/01431161.2025.2450567

Taylor & Francis
Taylor & Francis Group

Assessing optical water types in Asian coastal ocean waters from space using GCOM-C/SGLI observations

Eko Siswanto [a,b]

[a]Research Institute for Global Change (RIGC), Japan Agency for Marine-Earth Science and Technology (JAMSTEC), Yokohama, Japan; [b]Advanced Institute for Marine Ecosystem Change (WPI-AIMEC), Yokohama, Japan

ABSTRACT

Human activities and climate change exert environmental and ecological pressures on the Asian coastal ocean waters through dramatic changes in optical water types. This necessitates the development of methods to observe and monitor optical water types with optimal spatiotemporal resolution, which can only be achieved through remote sensing techniques, particularly for optically detectable water properties. This study utilized 250-mresolution ocean colour data retrieved from the Second-Generation Global Imager (SGLI), covering waters across Asia, to develop a common optical water type algorithm for Asian coastal ocean waters. The algorithm is based on relationships among optical properties, threshold values, and criteria, classifying the waters into eight optical water types: turbid, high-coloured-dissolved organic matter (CDOM), mixed, oligotrophic, coccolithophore bloom, mesotrophic, diatom bloom, and dinoflagellate bloom waters. The values of remote sensing reflectance (Rrs) slope between 490 and 530 nm (3.0×10^{-6}) and the Rrs at 490 nm (0.0013 sr^{-1}) serve as optimal thresholds for distinguishing dinoflagellate blooms, diatom blooms, and high-CDOM waters. The proposed method performs well in classifying most water bodies, though some artefacts suggest that refinements are needed to improve the method's robustness. The ability to classify optical water types provides a valuable tool for marine ecosystem and biogeochemical studies, especially in optically complex water bodies where land–ocean interactions are particularly strong.

ARTICLE HISTORY
Received 21 October 2024
Accepted 23 December 2024

Highlights

- Human activities and climate change alter optical water types in the Asian coastal ocean waters, necessitating optimal spatiotemporal satellite-based observations.
- This study develops an optical water type algorithm for Asian coastal ocean waters, designed for use with the GCOM-C/SGLI ocean colour sensor.
- The algorithm effectively classifies Asian coastal ocean waters into eight types of optical water properties.

CONTACT Eko Siswanto ekosiswanto@jamstec.go.jp Japan Agency for Marine-Earth Science and Technology (JAMSTEC), Research Institute for Global Change, 3173-25 Showa-machi, Kanazawa Ward, Yokohama, Kanagawa 236-0001, Japan

1. Introduction

Currently, around 40% of Asia's population resides within 100 km of the coast. The concentration of human settlements in coastal areas is driven by the economic benefits provided by multiple industries such as mariculture, tourism and recreation. However, the growing population and intense economic activities in these regions are putting increasing pressure on coastal ocean ecosystems, as evidenced by significant changes in water quality. Environmental pressures related to these changes include sedimentation, increases in dissolved organic and inorganic matter, eutrophication, red tides and hypoxia. These water quality shifts result in industrial damage, ecosystem and biodiversity loss, fish mortality, significant economic and livelihood losses, and adverse societal impacts. With climate change and global warming, these water quality issues are expected to worsen, further threatening marine life and food security by impairing fisheries production.

The United Nations (UN) places significant emphasis on coastal ocean water quality as a key indicator for measuring progress towards the Sustainable Development Goals (SDGs). This is particularly evident in Goal 14: Life Below Water, which focuses on conserving and sustainably using oceans, coastal waters, and marine resources for sustainable development. Specifically, the UN identifies eutrophication as indicator 14.1.1, which can lead to red tide events. The UN also directly links red tides to climate change in both the IPCC 5th Assessment Report (AR5) and the IPCC 2019 Special Report. Many Asian coastal ocean waters experience long-term and periodic changes in water quality, associated with emerging issues such as nutrient enrichment, red tide outbreaks, and sedimentation. This is due to the dense populations surrounding these waters (e.g. Guilmoto and Oliveau 2018) and their vulnerability to climate change, given their location between the Pacific and Indian Oceans (Siswanto et al. 2020).

Jakarta Bay, Manila Bay, the upper Gulf of Thailand, Chinese coastal waters, and Tokyo Bay (e.g. Feng et al. 2020; Luang-On et al. 2023) are among the coastal areas in Asia heavily affected by riverine effluent rich in dissolved organic and inorganic matter, leading to nutrient enrichment. As a result, these coastal oceans frequently experience eutrophication, red tides, and hypoxic conditions, causing severe damage to marine ecosystems, fisheries resources, and significant socioeconomic impacts. This situation calls for rapid coastal water quality monitoring to support efforts in mitigating and adapting to these changes. However, in situ monitoring is costly and impractical for long-term observation on a large spatiotemporal scale. Such large-scale and rapid observations can only be effectively achieved through satellite remote sensing.

The colour, or apparent optical properties of the coastal ocean, can serve as a measure of optical water quality, attributed to the amounts of in-water substances with unique light absorption and/or backscattering properties. In-water substances such as phytoplankton, total suspended solids (TSS, mg l^{-1}), and coloured-dissolved organic matter (CDOM) determine optical water types such as clear-blue waters, TSS-dominated turbid waters, and other optical water types (Moore, Campbell, and Dowell 2009; Moore, Dowell, and Franz 2012). In this study, 'optical water types' refer to categories of in-water substances that dominated the water optical properties that, at a primary level, can be qualitatively assessed by satellite ocean colour sensors through observed apparent optical properties—i.e. properties dependent on both the medium

and ambient lights (e.g. Chen, Zhang, and Guan 2018). To fully harness the potential of satellite remote sensing for monitoring coastal optical water types across Asia, it is essential to develop a common algorithm based on satellite data, particularly with optimal spatial resolution, as these optical water type changes typically occur in small coastal areas and embayments.

This study aims to develop a common algorithm to assess optical water types in coastal oceans across Asia. It utilizes multispectral ocean colour data with a 250-m spatial resolution, observed by the Second-Generation Global Imager (SGLI) onboard the Japanese Global Change Observation Mission (GCOM/C) satellite. This study presents an approach to mapping optical water types across the Asian coastal ocean waters with the optimal resolution – offering finer spatial resolution than the Aqua/MODIS, Suomi-NPP/VIIRS, and Sentinel-3/OLCI, as well as finer temporal and spectral resolutions than Landsat-8 and Sentinel-2. Unlike geostationary satellites or sensors (e.g. GOCI-II, Gaofen-4), this approach is globally scalable because GCOM-C is a sun-synchronous satellite.

2. Methodology

2.1. Site selection and rationale

To develop a common ocean colour algorithm applicable to the SGLI for assessing optical water types across Asian coastal ocean waters, this study followed the approach described by Siswanto et al. (2013) and Siswanto et al. (2024). The approach was designed to classify turbid water with high TSS, clear open oceans with low chlorophyll-a concentration (Chl-a, mg m^{-3}), and waters dominated by phytoplankton. The waters dominated by phytoplankton were further separated into diatom bloom or dinoflagellate bloom. Mixed waters interfering with CDOM were also classified. However, both approaches proposed by Siswanto et al. (2013) and Siswanto et al. (2024) were local algorithms, limiting their applicability to the entire Asian coastal ocean waters. To ensure broader applicability, SGLI data from various study sub-regions, as shown in Figure 1, were used.

The study sub-regions are the Arabian Sea (AraS), Bay of Bengal (BoB), southeastern Indian Ocean (SEIO), Malacca Strait (MS), South China Sea (SCS), Manila Bay (ManB), Jakarta Bay (JakB), upper Gulf of Thailand (uGoT), East China Sea (ECS), Bohai Sea (BoS), Yellow Sea (YeS), Tokyo Bay (TokB), Sagami Bay (SaB), southeast of Hokkaido (SeaHok), and Northern Caroline (NorCar). The sites were selected to represent a diverse and continuous range of bio-optical water properties, from end-members such as low-Chl-a waters in the open ocean to high-TSS or turbid waters, high-CDOM waters, and high-Chl-a waters or phytoplankton blooms. Additionally, the waters with phytoplankton blooms were further classified based on different types of phytoplankton blooms (Table 1).

2.2. GCOM-C/SGLI data acquisition and extraction

This study utilized the SGLI Level-2 dataset, incorporating the latest Version 3 atmospheric correction (Murakami et al. 2022; Toratani, Ogata, and Fukushima 2021). The dataset includes remote sensing reflectance (Rrs, sr^{-1}) and Chl-a at a spatial resolution of 250 m. The Chl-a and Rrs values were converted from their digital numbers using the provided scale factors and offset values. A detailed explanation of the Rrs

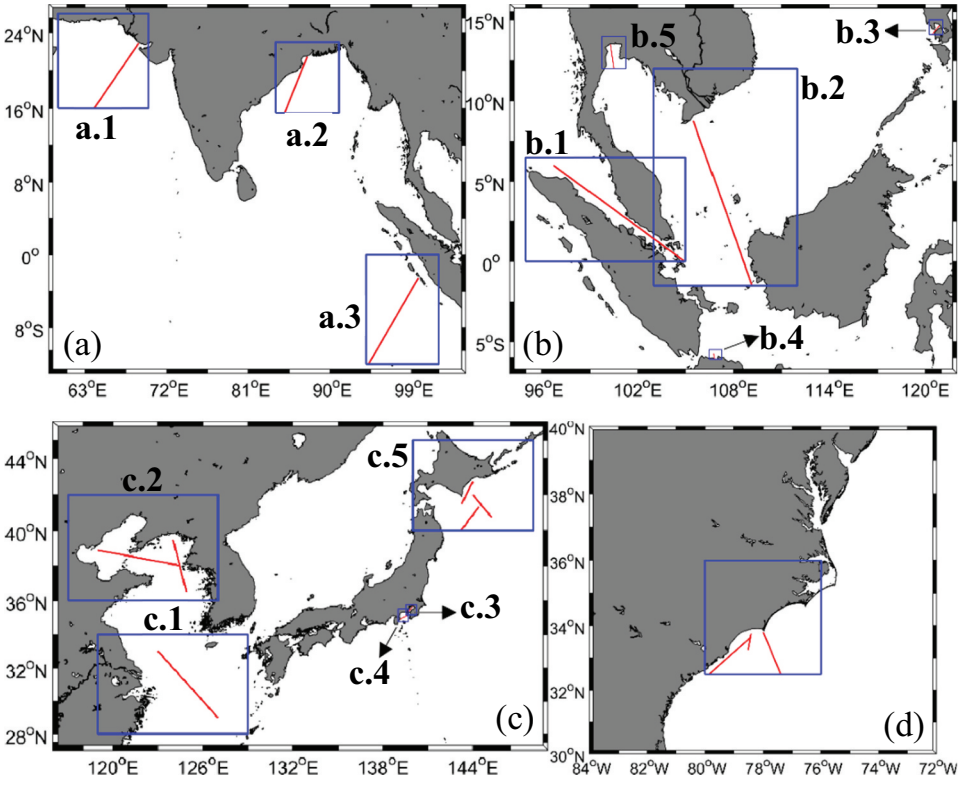

Figure 1. Geographic maps showing the sub-regions of this study. The blue boxes denote the sub-regions, while the red lines indicate the transect lines where SGLI-retrieved Chl-a and Rrs were extracted. (a) Sub-regions on the Indian Ocean side include the AraS (a.1), BoB (a.2), and SEIO (a.3). (b) Sub-regions in Southeast Asian coastal ocean waters include the MaS (b.1), SCS (b.2), ManB (b.3), JakB (b.4), and the uGoT (b.5). (c) Sub-regions on the Pacific Ocean side include the ECS (c.1), BoS and YeS (c.2), TokB (c.3), SaB (c.4), and off SeaHok (c.5). (d) The sub-region of NorCar in the Atlantic Ocean side.

computation, including the bidirectional reflectance distribution function correction, is available in Toratani, Ogata, and Fukushima (2021). The SGLI data were obtained from the Japan Aerospace Exploration Agency (JAXA) via G-Portal (JAXA – G-Portal, https://gportal.jaxa.jp/gpr/).

The Chl-a and Rrs data were extracted from the red transect lines in the study sub-regions (Figure 1). The Chl-a and Rrs values along these transect lines were defined as the mean values averaged from 3×3 pixel grids. Quality assurance (QA) flags – DATAMISS, LAND, ATMFAIL, CLDICE, STRAYLIGHT, and HIGLINT – were applied to ensure data quality. Detailed descriptions of these QA flags are available at: https://suzaku.eorc.jaxa.jp/GCOM_C/data/update/Algorithm_IWPR_en.html. The SGLI observes Rrs at seven wavelengths ($\lambda = 380$, 412, 443, 490, 530, 565 and 670 nm) in the UV-visible electromagnetic spectrum. However, due to the presence of negative values and low accuracy for Rrs at the UV band (380 nm) (hereafter Rrs_{380}, and Rrs_{λ} for other wavelengths), this study excluded Rrs_{380} from the analysis. A total of 2,423 Rrs spectra were extracted from all red transect lines, representing a broad range of water optical properties.

Table 1. Names of the study sub-regions selected for this research, along with their corresponding short names. The table 1 also includes the observation dates by GCOM-C/SGLI and descriptions of the expected or confirmed optical water types.

Sub-region	Short name	Observation date	Consideration/ confirmation
Arabian Sea	AraS	3 January 2024	No presumption
Bay of Bengal	BoB	19 July 2022	No presumption
Southeastern Indian Ocean	SEIO	2 December 2023	Phytoplankton bloom due to upwelling associated with 2023 El Niño
Malacca Strait	MaS	1 July 2021	Well-known turbid water (Tan et al. 2006)
South China Sea	SCS	25 January 2024	No presumption
Manila Bay	ManB	23 December 2020	Presumed to be optically complex water attributed to riverine organic and nutrient loading from untreated wastes (Manuel et al. 2021)
Jakarta Bay	JakB	30 March 2024	Presumed to be optically complex water attributed to riverine organic and nutrient loading from untreated wastes
Upper Gulf of Thailand	uGoT	10 January 2022	Well-known to be optically complex and eutrophic water due to riverine nutrient load (e.g. Luang-On et al. 2023)
East China Sea	ECS	30 January 2021	Well-known turbid water especially in winter due to intense wind-driven vertical mixing (Yamaguchi et al. 2013)
Bohai Sea	BoS	30 January 2022	Well-known turbid water especially in winter due to intense wind-driven vertical mixing (Wang et al. 2019)
Yellow Sea	YeS	30 January 2022	Well-known turbid water especially in winter due to intense wind-driven vertical mixing (Wang et al. 2019)
Tokyo Bay	TokB	17 July 2023	Well-known to be optically complex water attributed to riverine effluent rich in CDOM (Furukawa 2015; Higa et al., 2020; Kubo et al. 2023)
Sagami Bay	SaB	17 May 2020	Confirmed phytoplankton coccolithophore bloom (Yano et al. 2024)
Southeast Hokkaido	SeaHok	13 October 2021	Confirmed red tide caused by phytoplankton from the dinoflagellate group (Kuroda et al. 2022; Siswanto et al. 2024)
		8 May 2022	Expected to be seasonal blooms of phytoplankton diatom
		7 May 2022	Expected to be seasonal blooms of phytoplankton diatom
Northern Caroline	NorCar	28 September 2018	Confirmed to be optically complex water due to riverine effluent rich in CDOM following Hurricane Florence landfall (Paerl et al. 2020)

2.3. Data analysis

To group the 2,423 extracted Rrs spectra into clusters, this study applied hierarchical cluster analysis. The Euclidean distance was calculated to determine the similarity or dissimilarity between each pair of Rrs spectra. Ward's algorithm was applied to the squared Euclidean distances to assess the proximity of the Rrs spectra (Ward 1963). The agglomerative Ward's algorithm, also known as the minimum variance algorithm, is a linkage method based on variance analysis that minimizes the sum of squares within each cluster to evaluate the distance between them.

This study followed and expanded upon the approach proposed by Siswanto et al. (2013) and Siswanto et al. (2024), which used the relationship between the Rrs spectral slope between the blue (443 nm) and green (565 nm) wavelengths (hereafter $\mathrm{Rrs\_slope}_{443\_565}$) and Chl-a. This relationship has been effective in distinguishing between low-Chl-a waters, turbid waters with high non-phytoplankton inorganic particulate matter, and high-Chl-a waters, which may include seasonal phytoplankton blooms or blooms associated with red tide events. Threshold values and regression-based borderline expressions were then applied to further differentiate other optical water types, such as those influenced by different phytoplankton groups, CDOM-laden waters, and mixed waters.

3. Results

3.1. Association between eRGB and in-water substances

Pairs of enhanced red-green-blue composite (eRGB, left) and Chl-a (right) images in the study sub-regions are shown in Figure 2. Following the approach of Hu et al. (2005), the eRGB was generated using normalized water-leaving radiance (nLw, W m^{-2} sr^{-1} μm^{-1}) of three SGLI bands (565, 490 and 443 nm). Rrs was not used to create the eRGB composite image, as low Rrs values (where nLw is typically greater than 150 times Rrs) resulted in dark eRGB image. Collocations of vivid eRGB and high Chl-a can particularly be seen in the coastal waters of AraS (Figure 2(a.1)), BoB (Figure 2(a.2)), MaS (Figure 2(b.1)), SCS (Figure 2(b.2)), ECS (Figure 2(c.1)), BoS (Figure 2(c.2)), and SaB (Figure 2(c.4)). Reddish eRGB colours co-located with high Chl-a were observed especially in TokB (Figure 2(c.3)) and the SeaHok (Figure 2(c.5.1)). Additionally, brownish and dark-brown eRGB colours, accompanied by high Chl-a, were noted in the SeaHok (Figures 2(c.5.2, c.5.3)) and NorCar (Figure 2(d)), respectively.

The vivid eRGB in the MaS (Figure 2(b.a)) can be associated with turbid waters or high TSS, primarily consisting of non-phytoplankton particulate inorganic matter. In this study, TSS refers to suspended matter dominated by non-phytoplankton particulate inorganic material. It is well known that satellite-retrieved Chl-a in the MaS overestimates in situ Chl-a (Tan et al. 2006). This overestimation is caused by the significant presence of TSS. Vivid eRGBs observed during winter (30 January 2021) in the BoS, YeS, and ECS (Figures 2(c.1, c.2)) can also be attributed to high TSS. Strong winter winds drive vertical mixing, resuspending sediment from the sea bottom and increasing TSS. Yamaguchi et al. (2013) and Wang et al. (2019) reported that TSS caused a systematic overestimation of satellite-retrieved Chl-a in the ECS, BoS, and YeS during winter. Vivid eRGB was also observed in the SaB, but it was accompanied by moderate Chl-a (Figure 2(c.4)). Yano et al. (2024) recently found that the vivid colour observed on 17 May 2020 was due to a bloom of coccolithophores, a group of phytoplankton that produce calcium carbonate coccoliths (scales).

The reddish colour of eRGB observed in the waters off SeaHok (Figure 2(c.5.1)), collocated with high Chl-a, was identified as red tide waters caused by a bloom of phytoplankton from the dinoflagellate group (e.g. Kuroda et al. 2022; Siswanto et al. 2024). This red tide, which occurred in the fall of 2021, resulted in the severe mortality of salmon and sea urchins, causing significant economic losses totalling USD 70 million for local fisheries industries (Taniuchi et al. 2023). The brownish eRGB and high Chl-a observed in the spring (7–8 May 2022) in the waters off SeaHok (Figures 2(c.5.2, c.5.3)) were likely associated with a seasonal spring bloom, typically due to a bloom of phytoplankton from the diatom group. Coastal upwelling is well known to occur in the SEIO during El Niño years, leading to phytoplankton blooms (e.g. Siswanto 2015; Siswanto et al. 2020). These blooms in the upwelling waters are usually dominated by diatoms (e.g. Hutchings et al. 1995). Romero, Rixen, and Herunadi (2009) also reported an increase in diatom phytoplankton during 2002 El Niño in the SEIO. Therefore, diatom blooms are also expected to occur in the SEIO (Figure 2(a.3)) during the strong El Niño of 2023.

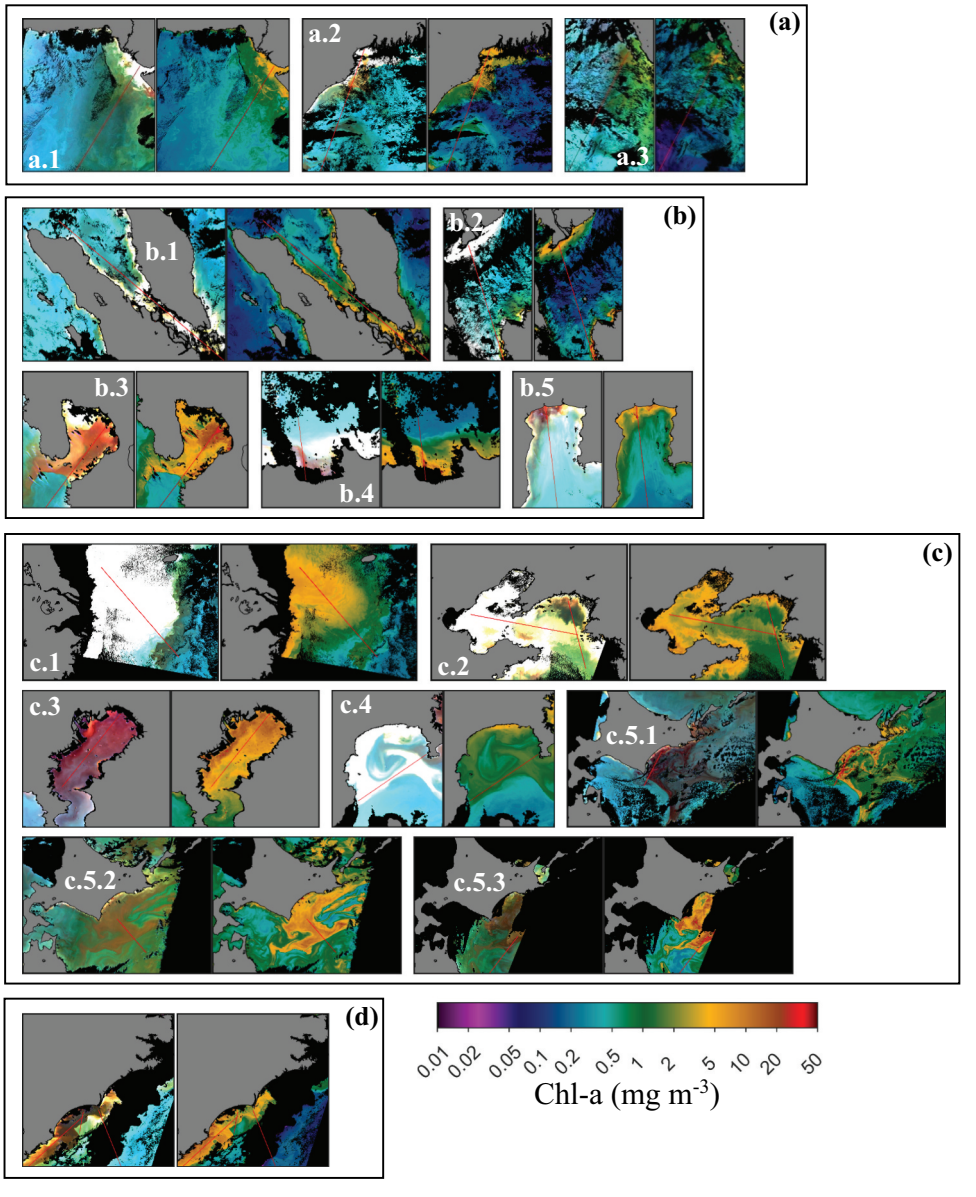

Figure 2. Pairs of eRGB (left) and Chl-a (right) images from the study sub-regions mentioned in Figure 1. The eRGB images were created by compositing nLw at 565 nm, 490 nm, and 443 nm following Hu et al. (2005). The red lines represent the transect lines from which the Rrs values were extracted and used for cluster analysis.

The dark brown eRGB, accompanied by high Chl-a in the coastal waters of NorCar (Figure 2(d)), was observed on 28 September 2018, 2 weeks after the landfall of extreme Hurricane Florence (14 September 2018). Paerl et al. (2020) reported a twofold increase in CDOM in the coastal waters of NorCar two weeks after Hurricane Florence's landfall. The dark brown eRGB was thus associated with high CDOM discharged by river flow.

3.2. Classifying water optical properties in oligotrophic-mesotrophic waters

A total of 2,423 Rrs spectra (Figure 3(a)) were extracted from all red transect lines shown in Figure 1. Cluster analysis divided the Rrs spectra into 21 clusters (C-1 to C-21), as shown in Figure 3(b). A scatter plot of $Rrs\_slope_{443\_565}$ against Chl-a (Figure 4) was created to demonstrate how the different optical properties of the waters and the clusters of Rrs spectra relate to Chl-a.

The Rrs spectra marked by the yellow circle in their graphs (C-8 – C-12, C-15, C-18 and C-20, Figure 3) showed remarkable peaks at 565 nm, moderate peaks at 530 nm, and low Rrs at 412 nm. These Rrs spectra were extracted from turbid waters, primarily from the ECS, BoS, MaS and AraS coastal waters. The group of clusters marked by a blue circle (C-1, C-2, C-5, C-6, C-13, C-16, C-21 and C-19), which exhibited gradual changes in Rrs at 412 nm, were extracted from clear waters with low Chl-a, located mainly in the open ocean regions of AraS, BoB, SEIO and SCS. Cluster C-14 (marked by a green circle), characterized by low Rrs at all wavelengths, mainly represented waters optically dominated by phytoplankton and/or CDOM. Two clusters C-7 and C-17 (marked by a brown circle), characterized by low Rrs_{412} and low peaks at 530 nm or 565 nm, primarily belonged to embayment and coastal waters such as the ManB, JakB, the uGoT and NorCar coastal waters. The Rrs spectra from the coccolithophore bloom that occurred in the SaB on 17 May 2020 were grouped into two clusters (C-3 and C-4), marked by a light blue circle. The Rrs cluster C-14 (phytoplankton and/or CDOM-dominated) was distinguishable from C-17 by its relatively lower Rrs peak at 565 nm. This suggests that cluster C-17, along with cluster C-7, was significantly influenced by TSS interference.

Following the approaches of Siswanto et al. (2013) and Siswanto et al. (2024), a scatter plot of $Rrs\_slope_{443\_565}$ against Chl-a (Figure 4) was created, and a regression line of Equation (1)

$$Rrs\_slope_{443\_565} = 0.00002 \times ln(Chl - a) + 0.00002 \quad (1)$$

is proposed as a borderline to separate turbid waters with high TSS from other optical water types. Data with a $Rrs\_slope_{443\_565}$ higher than that of Equation (1) represent turbid waters. Data with a $Rrs\_slope_{443\_565}$ lower than that of Equation (1) consist of low-to-moderate Chl-a, phytoplankton blooms, high CDOM, and mixed waters. Mixed waters were classified based on their location within the scatter plot, positioned between those representing turbid waters and those dominated by phytoplankton or high CDOM.

It is essential to classify coastal oceans based on (Chl - a) to indicate their productivity, trophic status, and the risk of suffering from eutrophication and red tide events. Previous studies have defined the trophic status of coastal oceans using different ranges of Chl-a (Hagy et al. 2022; O'Reilly and Werdell 2019; Sathishkumar et al. 2022). This study redefines oligotrophic (<1 mg m^{-3}), mesotrophic (1–5 mg m^{-3}), and eutrophic (>5 mg m^{-3}) waters based on new ranges of Chl-a that simplify and incorporate the ranges mentioned in previous studies (Figure 4).

It is worth noting that data from phytoplankton coccolithophore blooms fall within the mesotrophic waters category (1–5 mg m^{-3}). The Rrs spectra from coccolithophore blooms are characterized by moderate Rrs peaks at 490 nm and relatively higher Rrs_{412} compared to those from turbid waters (Figure 3). By exploiting these Rrs spectral characteristics,

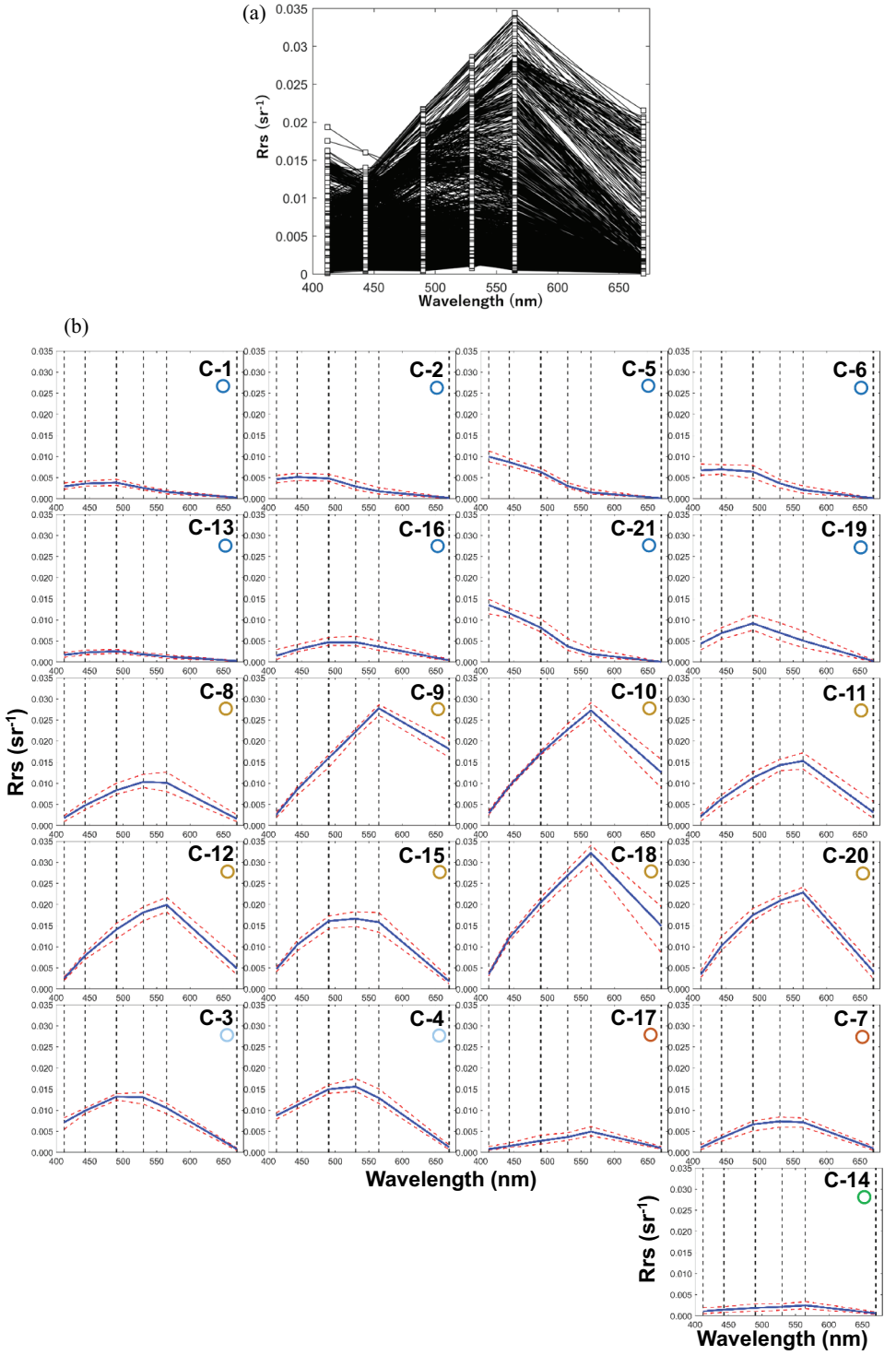

Figure 3. (a) A total of 2,423 Rrs spectra were extracted from all red transect lines in the study sub-region. (b) The 21 clusters (C-1 – C-21) of Rrs spectra resulted from the cluster analysis. In each graph, the blue line represents the mean Rrs spectrum, with the 10^{th} (red dashed lower line) and 90^{th} (red

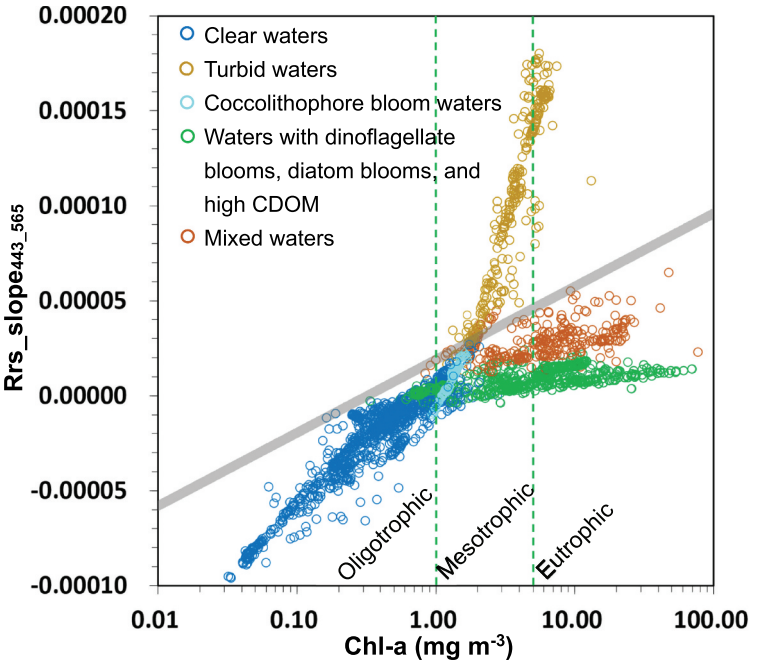

Figure 4. Scatter plot of $Rrs\_slope_{443\_565}$ against Chl-a for all clusters resulting from the cluster analysis. Data in dark blue and dark yellow represent various clusters corresponding to clear waters and turbid waters, respectively. Data in bright blue represent clusters associated with waters containing coccolithophore blooms. Data in green represent clusters associated with waters containing dinoflagellate blooms, diatom blooms, and high CDOM (see Figure 3 for the clusters of Rrs from the cluster analysis). Data in brown represent clusters corresponding to mixed waters. The dashed line, with equation (1) ($Rrs\_slope_{443\_565} = 0.00002 \times \mathrm{Ln}(\text{Chl-a}) + 0.00002$), is a regression line that separates clusters of turbid waters from clusters of other water types. The two vertical dashed green lines divide the trophic status of waters based on Chl-a: oligotrophic (<1 mg m^{-3}), mesotrophic (1–5 mg m^{-3}), and eutrophic (>5 mg m^{-3}) waters.

a scatter plot of the Rrs slope difference (Rrs_slope_{diff}, i.e. $Rrs\_slope_{490\_530}$ minus $Rrs\_slope_{412\_443}$) against Rrs_{412} was generated to differentiate coccolithophore bloom waters from other optical water types of mesotrophic waters (Figure 5(a)). Data with a Rrs_slope_{diff} higher than the values along the borderline expressed by Equation (2) below

$$Rrs\_slope_{diff} = -0.0937 \times Rrs_{412} + 0.0005 \quad (2)$$

dashed upper line) percentiles. The vertical dashed black lines indicate the SGLI wavelengths (412, 443, 490, 530, 565 and 670 nm). The colours of the circles below the cluster labels correspond to those shown in Figure 4. Clusters marked by dark blue and dark yellow circles consist of Rrs spectra representing clear waters and turbid waters, respectively. Clusters marked by bright blue circles (C-3 and C-4) consist of Rrs spectra from waters with coccolithophore blooms. Clusters marked by brown circles (C-7 and C-17) consist of Rrs spectra from mixed waters. The cluster marked by a green circle (C-14) consists of Rrs spectra from waters with dinoflagellate blooms, diatom blooms, and high CDOM.

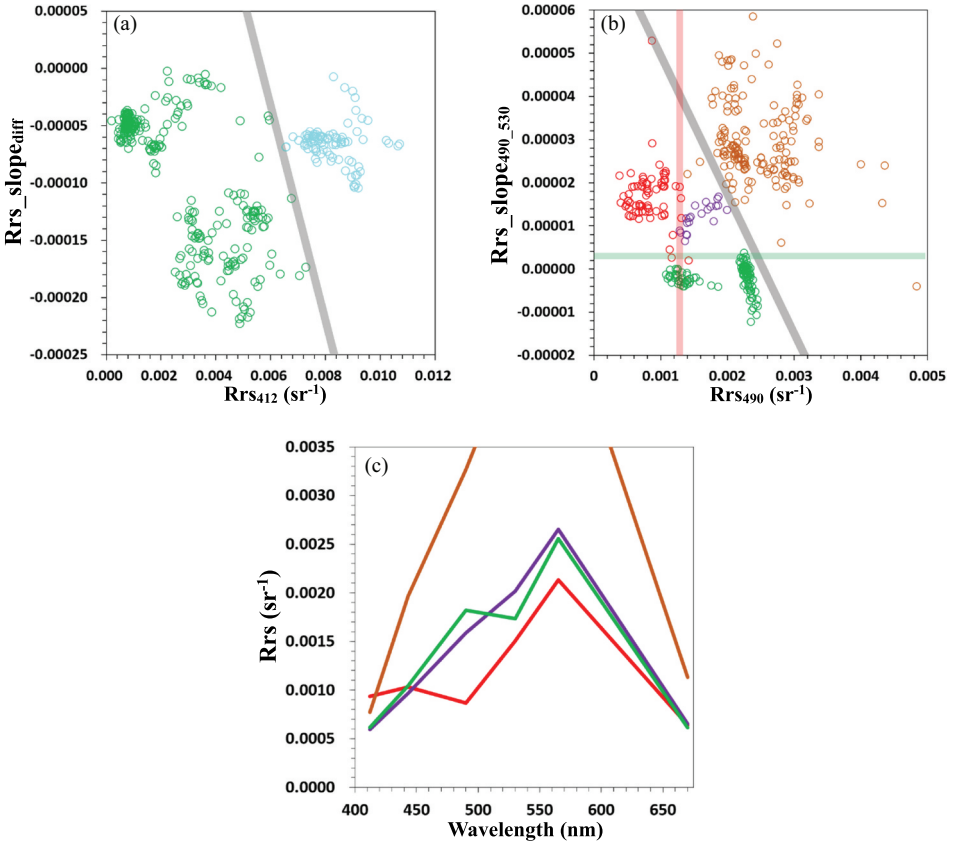

Figure 5. (a) Scatter plot of Rrs_slope$_{diff}$ against Rrs$_{412}$. The grey line in (a) is a regression line (Equation (2): Rrs_slope$_{diff}$ = −0.0973 × Rrs$_{412}$ + 0.0005), which separates clusters representing coccolithophore bloom waters (light blue circles) from other clusters within mesotrophic waters (Chl-a of 1–5 mg m^{-3}), where Rrs_slope$_{diff}$ = Rrs_slope$_{490_530}$ − Rrs_slope$_{412_443}$. (b) Scatter plot of Rrs_slope$_{490_530}$ against Rrs$_{490}$. The grey line in (b), expressed by equation (3) (Rrs_slope$_{490_530}$ = −0.0322 × Rrs$_{490}$ + 0.00008), serves as a borderline separating mixed waters (brown circles) from other optical water types (green, red, and purple cirles representing diatom bloom, dinoflagellate bloom, and high-CDOM waters, respectively) within eutrophic waters (Chl-a > 5 mg m^{-3}). (c) The mean Rrs spectra for mixed waters (brown), diatom bloom waters (green), dinoflagellate bloom waters (red), and high-CDOM waters (purple).

are classified as coastal oceans experiencing phytoplankton coccolithophore blooms. The remaining non-coccolithophore bloom data in mesotrophic waters are simply classified as waters with moderate Chl-a, ranging from 1 to 5 mg m^{-3}.

3.3. Classifying water optical properties in eutrophic waters

Previous studies have used a threshold of satellite-retrieved Chl-a >5 mg m^{-3} to classify waters as being susceptible to eutrophication (Maúre et al. 2021) and red tide outbreaks

(Shang et al. 2014). The same threshold (Chl-a >5 mg m^{-3}) is applied in this study when classifying the bloom-causing phytoplankton types (diatom or dinoflagellate).

Figure 5(b) shows a scatter plot of $Rrs\_slope_{490\_530}$ against Rrs_{490} derived from all data with Chl-a greater than 5 mg m^{-3}, excluding the data previously classified by Equation (1) as turbid waters with high TSS. The reasons for selecting $Rrs\_slope_{490\_530}$ and Rrs_{490} as variables for the scatter plot are as follows: 1) contrasting slopes of diatom blooms (negative) against dinoflagellate blooms (positive); and 2) high Rrs_{490} during diatom blooms but low Rrs_{490} during dinoflagellate blooms (Figure 5(c)). Notably, mixed waters are grouped separately (Figure 5(b)) above the grey regression line of Equation (3)

$$Rrs\_slope_{490\_530} = -0.0322 \times Rrs_{490} + 0.00008 \quad (3)$$

below which are the data belonging to diatom blooms, dinoflagellate blooms, and high CDOM. The mean Rrs from mixed waters exhibited high values at green wavelengths (Figure 5(c)), indicating a mixture with turbid waters. Higher Rrs during diatom blooms compared to dinoflagellate blooms (Figure 5(c)) is consistent with in situ hyperspectral Rrs measurements reported by Shang et al. (2014). Higher $Rrs\_slope_{443\_490}$ during diatom blooms, relative to dinoflagellate blooms, is also consistent with Shang et al. (2014) results. However, this study did not utilize $Rrs\_slope_{443\_490}$, as its similarity (high positive slope values) in both diatom bloom and high-CDOM waters made it difficult to distinguish between the two. While classifying mixed waters is relatively straightforward, it is challenging to discriminate between waters with diatom blooms, dinoflagellate blooms, and high CDOM.

The scatter plot in Figure 5(b) is particularly useful for distinguishing waters with diatom blooms from those with dinoflagellate blooms. Data associated with diatom blooms tend to have low $Rrs\_slope_{490\_530}$, which can be approximately separated using an $Rrs\_slope_{490\_530}$ threshold value of less than 0.000003. Following the discrimination of diatom bloom waters, dinoflagellate bloom waters can be approximately separated using an Rrs_{490} threshold value of less than 0.0013 sr^{-1}. The remaining unclassified data are defined as waters with high CDOM, as they primarily originate from the NorCar coastal waters following the landfall of Hurricane Florence.

The aforementioned procedures classify water optically into eight types: 1) turbid waters with high TSS, 2) clear or oligotrophic waters with Chl-a <1 mg m^{-3}, 3) phytoplankton coccolithophore bloom waters, 4) mesotrophic waters with moderate Chl-a (1–5 mg m^{-3}), 5) mixed waters, 6) diatom bloom waters, 7) dinoflagellate bloom waters, and 8) high CDOM waters. The procedures, including the criteria and thresholds used for classification, are schematically summarized as a flowchart in Figure 6.

3.4. Geographical distribution of optical water types in the study sub-regions

Figure 7 presents maps of optical water types in the study sub-regions, classified using the proposed method. To facilitate comparisons between water classification results and their corresponding eRGB and Chl-a images, the figure indices in Figure 7 match those in Figure 2, regardless of their order of reference in this section.

Turbid or TSS-rich waters were identified mainly in the marginal seas of the ECS (Figure 7(c.1)), BoS (Figure 7(c.2)), northeastern coast of AraS (Figure 7(a.1)), northwestern coast of BoB (Figure 7(a.2)), coastal waters of the MaS (Figure 7(b.1)), northern coast of SCS

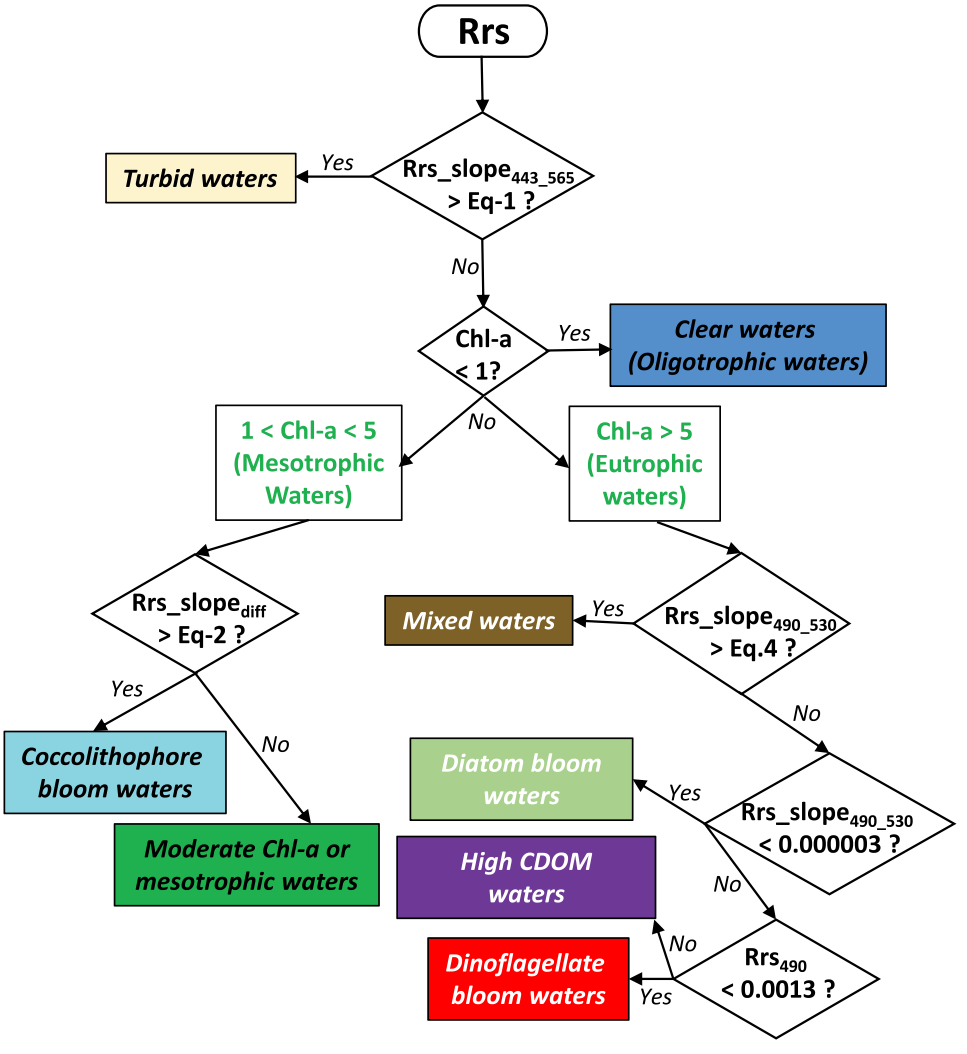

Figure 6. Flowchart outlining the method and criteria for classifying optical water types into eight categories: turbid waters, mixed waters, clear-oligotrophic waters, coccolithophore bloom waters, mesotrophic-moderate Chl-a waters, cdom-dominated waters, eutrophic-diatom bloom waters, and eutrophic-dinoflagellate bloom waters.

(Figure 7(b.2)), northern coast of ManB (Figure 7(b.3)), northeastern coast of uGoT (Figure 7(b.5)), and northern coast of SaB (Figure 7(c.4)). A large portion of mixed waters was identified in the ManB (Figure 7(b.3)), JakB (Figure 7(b.4)), TokB (Figure 7(c.3)), and along the southern coast of NorCar (Figure 7(d)). Waters with high CDOM were classified along the southern coast of NorCar and in TokB.

In the mesotrophic waters with Chl-a <5 mg m^{-3}, the presence of phytoplankton coccolithophores was identified in the SaB (Figure 7(c.4)). In the eutrophic waters with Chl-a >5 mg m^{-3}, blooms caused by phytoplankton from the dinoflagellate (Figure 7 (c.5.1)) and diatom (Figures 7(c.5.2, c.5.3)) groups were also identified. Waters with Chl-a

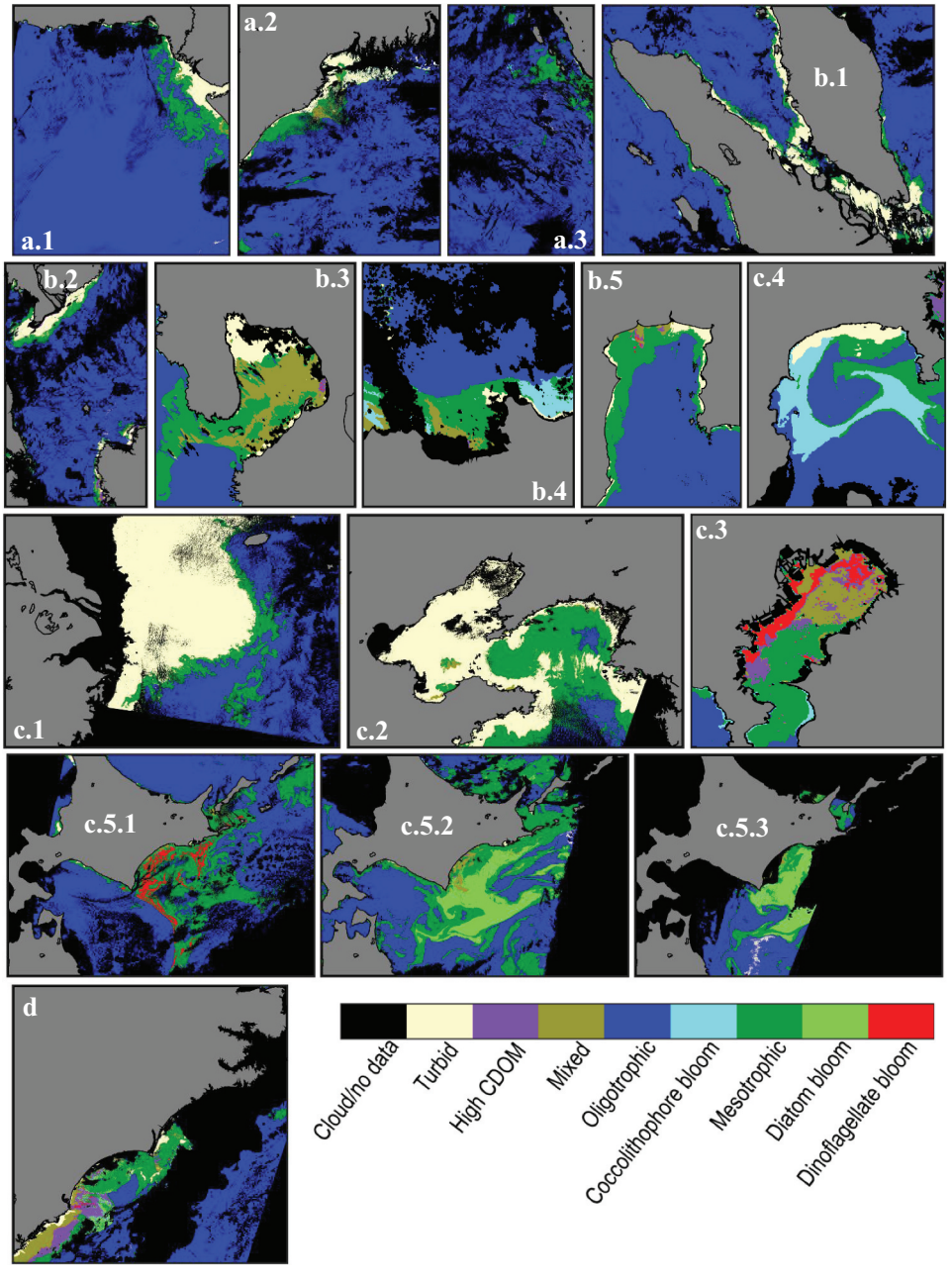

Figure 7. Maps of optical water types in the sub-regions of the study classified using the method outlined in Figure 6 proposed by this study. Eight optical water types are produced by the proposed method: turbid, high-cdom, mixed, oligotrophic, coccolithophore bloom, mesotrophic, diatom bloom, and dinoflagellate bloom waters.

ranging from 1 to 5 mg m^{-3}, other than those dominated by coccolithophores, were classified as mesotrophic for the sake of simplification and because they are unlikely to cause harmful effects within that Chl-a range. The rationale for the approach taken in this study will be discussed below as a guide for interpreting the results of optical water property classifications.

4. Discussion

4.1. Rationale and advantages of the optical water type classification interpretation

Turbid and clear waters can be classified with high likelihood by the scatter plot of $Rrs\_slope_{443\_565}$ against Chl-a (Figure 4). The vivid colours in the eRGB imagery provide self-validation for the presence of turbid water with high TSS, regardless of the magnitude of Chl-a. Waters with low Chl-a, particularly in the open ocean, are undoubtedly clear and oligotrophic. Defining clear water directly by referring to low Chl-a is more straightforward and certain compared to the approach that relies on Rrs spectral recognition (e.g. Siswanto et al. 2013, 2024). This is especially true because retrievals of Rrs in the short wavelengths by all ocean colour sensors are generally more prone to atmospheric correction issues and, therefore, more uncertain compared to those in the longer wavelengths.

Vivid colours in the eRGB imagery are, however, not always associated with turbid waters. The vivid eRGB observed in the SaB on 17 May 2020 was confirmed to be caused by the presence of phytoplankton coccolithophores (Yano et al. 2024). The method proposed here detected the presence of coccolithophores in mesotrophic waters (Figure 2(c.4)). In the northern coast of SaB, however, the vivid colour (Figure 2(c.4)) was classified as turbid waters, exhibiting a discrepancy with the results obtained using the flagging method demonstrated by Yano et al. (2024).

Interpreting the likely optical water types in mesotrophic waters (Chl-a range: 1–5 mg m^{-3}) is challenging. Although the current study does not classify optical water types in mesotrophic waters for the sake of simplicity and the expectation of no harmful effects, it is worthwhile to describe the rationales for interpreting the likelihood of these optical water types. The geographic location of classified mesotrophic waters and the main optical water types adjacent to them are important considerations when interpreting mesotrophic waters.

In offshore waters, the types of mesotrophic waters located adjacent to phytoplankton blooms caused by specific phytoplankton species or groups are likely the same as the main optical water types. For instance, during the events of dinoflagellate (Figure 7(c.5.1)) and diatom (Figure 7(c.5.2)) blooms (Chl-a >5 mg m^{-3}), the mesotrophic waters are likely extensions of the dinoflagellate and diatom blooms, albeit with lower bloom intensities associated with lower Chl-a (1–5 mg m^{-3}). Mesotrophic waters classified adjacent to coccolithophore waters (Figure 7(c.4)) were likely extensions of the main coccolithophore bloom waters.

A similar interpretation also applies to mesotrophic waters adjacent to main turbid waters, such as in the ECS (Figure 7(c.1)), BoS (Figure 7(c.2)), and MaS (Figure 7b.1). These mesotrophic waters are likely to contain moderate levels of TSS. However, detached

patches of mesotrophic waters from the main turbid waters might exhibit optical properties that differ from those of the surrounding turbid waters. For instance, the mesotrophic waters located southeast of the main turbid waters in the ECS and southwest of the main turbid waters in the AraS (Figure 7(a.1)) may be more associated with phytoplankton rather than TSS.

Understanding whether high Chl-a is optically more associated with high TSS or phytoplankton is essential for marine ecosystem and biogeochemical studies. Chl-a is commonly used to assess the status of eutrophication (Maúre et al. 2021; Terauchi et al. 2014), which is adopted by the United Nations for measuring progress towards Sustainable Development Goal 14: Life Below Water. Applying satellite Chl-a data that is interfered with by TSS (e.g. Wang et al. 2019; Yamaguchi et al. 2013) can result in an incorrect assessment of eutrophication status. Modelling phytoplankton primary production, particulate organic carbon flux and air-sea carbon dioxide flux in coastal oceans will also be problematic when erroneous satellite Chl-a data is used. The optical water type maps mentioned in Figure 7 can thus serve as a guide for marine ecosystems and biogeochemical studies in coastal oceans.

4.2. Challenging issues to be addressed

One issue identified in the classification results is the mesotrophic waters classified in the northern portion of the NorCar coastal waters (Figure 7(d)). Due to the criterion applied for classifying mesotrophic waters based on Chl-a that ranges from 1 to 5 mg m^{-3}, the waters that were expected to optically belong to post-hurricane CDOM-laden waters (based on their dark brown eRGB imagery) were simply classified as mesotrophic waters with moderate Chl-a (Figure 2(d)). This occurs because the classification approach used in this study emphasizes optical water types in eutrophic waters with Chl-a >5 mg m^{-3} due to the potential risk of red tide occurrences. However, as CDOM can lead to hypoxic conditions, which can be detrimental to marine organisms below the surface, it is recommended that future work includes water type classification in mesotrophic waters.

There is a discrepancy in the detection results of phytoplankton coccolithophores between this study and Yano et al. (2024). The area of coccolithophores detected in this study was smaller than that reported by Yano et al. (2024). They adopted nLw thresholds proposed by Iida et al. (2002, 2012) to classify the presence of phytoplankton coccolithophores when nLw at 443 nm (nLw_{443}) and 565 nm (nLw_{565}) are higher than 1.1 and 0.8 mW cm^{-2} μm^{-1} sr^{-1}, respectively. Such a flagging method appears to work properly in optically homogeneous waters where there is no significant interference from TSS. However, applying these thresholds alone led to the false classification of TSS-laden waters, such as those in the ECS and MaS, as coccolithophore bloom water types (data not shown). This occurred because the nLw_{443} and nLw_{565} in the turbid waters exceed Iida et al. (2002, 2012) nLw thresholds. Even when the thresholds of the three band ratios in Iida et al. (2002, 2012) were applied, less turbid waters were unexpectedly classified as coccolithophore bloom waters.

The current study's approach also classified the northern coast of the SaB as turbid waters. This classification is reasonable, as the Rrs values were high and peaked at 565 nm (data not shown), exhibiting common optical properties in optically complex waters with high TSS. However, the classification of turbid waters was also somewhat overestimated,

as the classified turbid waters exhibited Rrs peaks at 490 and 530 nm, which are typical optical properties of waters with coccolithophore blooms (e.g. Cazzaniga, Zibordi, and Mélin 2021; Moore, Dowell, and Franz 2012). A likely false coccolithophore bloom detection also occurred in the coastal waters east of JakB (Figure 7(b.4)). In future studies, an improved method capable of discriminating coccolithophore blooms from TSS-laden waters may involve identifying the wavelengths at which the Rrs peaks occur.

The northern portion of TokB is classified as an optically mixed water type (Figure 7(c.3)). It is likely due to the mixing of water with high Chl-a and riverine effluent rich in CDOM, as TokB is a highly urbanized, semi-enclosed water body (Furukawa 2015;; Kubo et al. 2023). The mixed water, characterized by high CDOM and high Chl-a, can be identified by patches of high CDOM waters and a phytoplankton bloom from the dinoflagellate group. The occurrence of red tide events, as indicated by elevated Chl-a levels, is reasonable because the image was taken during summer (17 July 2023), the peak season for red tides in TokB (e.g. Kusano, 2019). Unfortunately, there were no coinciding field observations of red tides to confirm the phytoplankton species responsible. However, based on the long-term data (2000–2017), Kusano (2019) reported that dinoflagellates are the second most frequent cause of red tides in TokB after diatoms.

The areas showing dinoflagellate phytoplankton blooms off SeaHok (Figure 7(c.5.1)) are approximately collocated with the areas of high dinoflagellate cell density reported by Kuroda et al. (2022). As discussed above, it is reasonable to expect that the mesotrophic waters (Chl-a range: $1 \sim 5$ mg m^{-3}) surrounding the main dinoflagellate blooms are extensions of the primary bloom but with lower intensity. This is supported by Kuroda et al. (2022) dinoflagellate cell density map (Figure 13 in Kuroda et al. 2022), which shows lower cell densities surrounding the main blooms. Although red tides are typically associated with Chl-a higher than 10 mg m^{-3} (e.g. Kuroda et al. 2022; Luang-On et al. 2023; Yunus, Dou, and Sravanthi 2015), Luang-On et al. (2024) recently found that red tides observed by the GCOM-C/SGLI sensor can exhibit Chl-a levels lower than 10 mg m^{-3}. Therefore, selecting a 5 mg m^{-3} Chl-a threshold to capture the main red tide areas is plausible, particularly when using GCOM-C/SGLI observations.

Classifying waters with Chl-a levels ranging from 1 to 5 mg m^{-3} simply as mesotrophic waters presents challenges, such as unclassified high-CDOM waters, the inability to distinguish between TSS-dominated and phytoplankton-dominated waters, and the inability to identify the dominant phytoplankton group within mesotrophic waters. The approaches used in this study primarily rely on Chl-a, thresholds, and regression lines derived from relationships observed among the water's optical properties. The robustness of these borderlines and threshold values largely depends on the size of the dataset used. It would be beneficial to improve the current method by incorporating additional datasets from other sub-regions to enhance its robustness. This study also recommends including criteria capable of classifying optical water types within mesotrophic waters. Future work should focus on identifying Rrs spectrum peaks (to distinguish coccolithophore blooms from turbid waters), defining thresholds and borderlines in mesotrophic waters (to classify high-CDOM waters and map areas with less intense blooms), and applying inherent optical property models (e.g. Siswanto et al. 2024) to differentiate diatom from dinoflagellate blooms.

5. Conclusions

This study proposes a method based on apparent water optical properties to assess optical water types across Asian coastal ocean waters, designed for use with the GCOM-C/SGLI ocean colour sensor. The relationships among optical properties, threshold values, and criteria form an ocean colour algorithm that classifies Asian coastal ocean waters into eight optical water types: turbid, high-CDOM, mixed, oligotrophic, coccolithophore bloom, mesotrophic, diatom bloom, and dinoflagellate bloom waters. The SGLI-derived $Rrs\_slope_{490\_530}$ of 3.0×10^{-6} and Rrs_{490} of 0.0013 sr^{-1} serve as the borderlines that separate dinoflagellate bloom, diatom bloom, and high-CDOM waters. Overall, the method performs well in classifying most coastal ocean waters, although some artefacts remain, requiring refinement in future studies. The ability to classify water optical types provides a valuable tool for marine ecosystem research and biogeochemical research.

Disclosure statement

No potential conflict of interest was reported by the author.

Funding

This research was supported by the Japan Aerospace Exploration Agency–3rd Research Announcement on the Earth Observations [JAXA–3rd EORA, contract: 24RT000233] and Grants-in-Aid for Scientific Research [KAKENHI JP21H05317] funded by the Ministry of Education, Culture, Sports, Science, and Technology-Japan (MEXT). This work was also partially supported by the Asia-Pacific Network for Global Change Research [APN, CRRP2024-05MY-Siswanto].

ORCID

Eko Siswanto http://orcid.org/0000-0002-8215-0082

References

Cazzaniga, I., G. Zibordi, and F. Mélin. 2021. "Spectral Variations of the Remote Sensing Reflectance During Coccolithophore Blooms in the Western Black Sea." *Remote Sensing of Environment* 264:112607. https://doi.org/10.1016/j.rse.2021.112607.

Chen, W., T. Zhang, and L. Guan. 2018. "8.02 - Radiation Transfer in the Ocean and Ocean Color." In *Shunlin Liang*, Comprehensive Remote Sensing, Editor(s). Elsevier. https://doi.org/10.1016/B978-0-12-409548-9.10397-5.

Dias, A, and S. Kurian. 2022. "Characterization of Colored Dissolved Organic Matter Along the Western Continental Shelf of India During the Seasonal Hypoxia." *Estuarine Coastal and Shelf Science* 265:107714. https://doi.org/10.1016/j.ecss.2021.107714.

Feng, C., J. Ishizaka, K. Saitoh, T. Mine, and H. Yamashita. 2020. "A Novel Method Based on Backscattering for Discriminating Summer Blooms of the Raphidophyte (*Chattonella* Spp.) and the Diatom (*Skeletonema* Spp.) Using MODIS Images in Ariake Sea, Japan." *Remote Sensing* 12 (9): 1504. https://doi.org/10.3390/rs12091504.

Furukawa, K. 2015. "Eutrophication in Tokyo Bay." In *Eutrophication and Oligotrophication in Japanese Estuaries.* Estuaries of the World, edited by T. Yanagi. Springer, Dordrecht. https://doi.org/10.1007/978-94-017-9915-7_2.

Guilmoto, C. Z., and S. Oliveau. 2018. "Population Distribution Across Asia." *Routledge Handbook of Asian Demography, Routledge* 9780415659901:268–284. https://hal.science/hal-01756485.

Hagy, J. D., B. J. Kreakie, M. C. Pelletier, F. Nojavan, J. A. Kiddon, and A. J. Oczkowski. 2022. "Quantifying Coastal Ecosystem Trophic State at a Macroscale Using a Bayesian Analytical Framework." *Ecological Indicators* 142:109267. https://doi.org/10.1016/j.ecolind.2022.109267.

Higa, H., S. Sugahara, S. I. Salem, Y. Nakamura, and T. Suzuki. 2020. "An Estimation Method for Blue Tide Distribution in Tokyo Bay Based on Sulfur Concentrations Using Geostationary Ocean Color Imager (GOCI)." *Estuarine Coastal and Shelf Science* 235:106615. https://doi.org/10.1016/j.ecss.2020.106615.

Hu, C., F. E. Muller-Karger, C. Taylor, K. L. Carder, C. Kelble, E. Johns, and C. A. Heil. 2005. "Red Tide Detection and Tracing Using MODIS Fluorescence Data: A Regional Example in SW Florida Coastal Waters." *Remote Sensing of Environment* 97 (3): 311–321. https://doi.org/10.1016/j.rse.2005.05.013.

Hutchings, L., G. C. Pitcher, T. A. Probyn, and G. W. Bailey. 1995. "The Chemical and Biological Consequences of Coastal Upwelling." In *Upwelling in the Oceans; Modern Processes and Ancient Records*, edited by C. P. Summerhayes, K.-C. Emeis, M. V. Angel, R. L. Smith, and B. Zeitschel, 65–81. New York: Wiley.

Iida, T., K. Mizobata, and S.-I. Saitoh. 2012. "Interannual Variability of Coccolithophore Emiliania Huxleyi Blooms in Response to Changes in Water Column Stability in the Eastern Bering Sea." *Continental Shelf Research* 34:7–17. https://doi.org/10.1016/j.csr.2011.11.007.

Iida, T., S. I. Saitoh, T. Miyamura, M. Toratani, H. Fukushima, and N. Shiga. 2002. "Temporal and Spatial Variability of Coccolithophore Blooms in the Eastern Bering Sea, 1998-2001." *Progress in Oceanography* 55 (1–2): 165–175. https://doi.org/10.1016/S0079-6611(02)00076-9.

Kubo, A., Y. Yamashita, F. Hashihama, and J. Kanda. 2023. "The Origin and Characteristics of Dissolved Organic Carbon in the Highly Urbanized Coastal Waters of Tokyo Bay." *Journal of Oceanography* 79 (3): 241–252. https://doi.org/10.1007/s10872-023-00678-5.

Kuroda, H., Y. Taniuchi, T. Watanabe, T. Azumaya, and N. Hasegawa. 2022. "Distribution of Harmful Algae (*Karenia* Spp.) in October 2021 off Southeast Hokkaido, Japan." *Frontiers in Marine Science* 9:841364. https://doi.org/10.3389/fmars.2022.841364.

Kusano, A. 2019. "Recent Outbreaks of Red Tide in Tokyo Bay." *Bulletin of the Kanagawa Prefectural Fisheries Research Institute* 10: 51–56. Accessed November 14. https://www.pref.kanagawa.jp/documents/11497/10-07kusano.pdf (in Japanese.

Luang-On, J., J. Ishizaka, A. Buranapratheprat, J. Phaksopa, J. I. Goes, E. R. Maúre, E. Siswanto, et al. 2023. "MODIS-Derived Green *Noctiluca* Blooms in the Upper Gulf of Thailand: Algorithm Development and Seasonal Variation Mapping." *Frontiers inMarine Science* 10:1031901. https://doi.org/10.3389/fmars.2023.1031901.

Luang-On, J., E. Siswanto, K. Ogata, M. Toratani, A. Buranapratheprat, D. Leenawarat, and J. Ishizaka. 2024. "Enhancing the Reliability of GCOM-C/SGLI Data for Red Tide Detection in the Upper Gulf of Thailand." *Remote Sensing Letters* 15 (10): 1096–1106. https://doi.org/10.1080/2150704X.2024.2406032.

Manuel, A., A. C. Blanco, O. Cabrera, and M. L. San Diego-McGlone. 2021. "Mapping Coloured Dissolved Organic Matter in Manila Bay Using Sentinel-3 and Wasi." *International Archives of the Photogrammetry, Remote Sensing and Spatial Information Sciences* XLVI-4/W6-2021:207–212. https://doi.org/10.5194/isprs-archives-XLVI-4-W6-2021-207-2021,2021.

Maúre, E. D. R., G. Terauchi, J. Ishizaka, N. Clinton, and M. DeWitt. 2021. "Globally Consistent Assessment of Coastal Eutrophication." *Nature Communications* 12 (1): 6142. https://doi.org/10.1038/s41467-021-26391-9.

Moore, T. S., J. W. Campbell, and M. D. Dowell. 2009. "A Class-Based Approach to Characterizing and Mapping the Uncertainty of the MODIS Ocean Chlorophyll Product." *Remote Sensing of Environment* 113 (11): 2424–2430. https://doi.org/10.1016/j.rse.2009.07.016.

Moore, T. S., M. D. Dowell, and B. A. Franz. 2012. "Detection of Coccolithophore Blooms in Ocean Color Satellite Imagery: A Generalized Approach for Use with Multiple Sensors." *Remote Sensing of Environment* 117:249–263. https://doi.org/10.1016/j.rse.2011.10.001.

Murakami, H., D. Antoine, V. Vellucci, and R. Frouin. 2022. "System Vicarious Calibration of GCOM-C/SGLI Visible and Near-Infrared Channels." *Journal of Oceanography* 78 (4): 245–261. https://doi.org/10.1007/s10872-022-00632-x.

O'Reilly, J. E., and P. J. Werdell. 2019. "Chlorophyll Algorithms for Ocean Color Sensors - OC4, OC5 & OC6." *Remote Sensing of Environment* 229:32–47. https://doi.org/10.1016/j.rse.2019.04.021.

Paerl, R. W., R. E. Venezia, J. J. Sanchez, and H. W. Paerl. 2020. "Picophytoplankton Dynamics in a Large Temperate Estuary and Impacts of Extreme Storm Events." *Scientific Reports* 10 (1): 22026. https://doi.org/10.1038/s41598-020-79157-6.

Romero, O. E., T. Rixen, and B. Herunadi. 2009. "Effects of Hydrographic and Climatic Forcing on Diatom Production and Export in the Tropical Southeastern Indian Ocean." *Marine Ecology Progress Series* 384:69–82. https://doi.org/10.3354/meps08013.

Sathishkumar, R. S., A. Sundaramanickam, A. K. Mohanty, G. Sahu, T. Ramesh, K. Balachandar, A. Nithin, P. Surya, and K. Silambarasan. 2022. "Seasonal Assessment of the Trophic Status in the Coastal Waters Adjoining Tuticorin Harbor in Relation to Water Quality and Plankton Community in the Gulf of Mannar, India." *Oceanologia* 64 (4): 749–768. https://doi.org/10.1016/j.oceano.2022.07.002.

Shang, S., J. Wu, B. Huang, G. Lin, Z. Lee, J. Liu, and S. Shang. 2014. "A New Approach to Discriminate Dinoflagellate from Diatom Blooms from Space in the East China Sea." *Journal of Geophysical Research: Ocean* 119 (7): 4653–4668. https://doi.org/10.1002/2014JC009876.

Siswanto, E. 2015. "Atmospheric Deposition—Another Source of Nutrients Enhancing Primary Productivity in the Eastern Tropical Indian Ocean During Positive Indian Ocean Dipole Phases." *Geophysical Research Letter* 41 (13): 5378–5386. https://doi.org/10.1002/2015GL064188.

Siswanto, E., T. Horii, I. Iskandar, J. L. Gaol, R. Y. Setiawan, and R. D. Susanto. 2020. "Impacts of Climate Changes on the Phytoplankton Biomass of the Indonesian Maritime Continent." *Journal of Marine Systems* 212:103451. https://doi.org/10.1016/j.jmarsys.2020.103451.

Siswanto, E., J. Ishizaka, S. C. Tripathy, and K. Miyamura. 2013. "Detection of Harmful Algal Blooms of Karenia Mikimotoi Using MODIS Measurements: A Case Study of Seto-Inland Sea, Japan." *Remote Sensing of Environment* 129:185–196. https://doi.org/10.1016/j.rse.2012.11.003.

Siswanto, E., J. Luang-On, K. Ogata, H. Higa, and M. Toratani. 2024. "Observations of Water Optical Properties During Red Tide Outbreaks off Southeast Hokkaido by GCOM-C/SGLI: Implications for the Development of Red Tide Algorithms." *Remote Sensing Letters* 15 (2): 121–132. https://doi.org/10.1080/2150704X.2024.2302948.

Tan, C. K., J. Ishizaka, S. Matsumura, F. M. Yusoff, and M. I. H. Mohamed. 2006. "Seasonal Variability of Seawifs Chlorophyll a in the Malacca Straits in Relation to Asian Monsoon." *Continental Shelf Research* 26 (2): 168–178. https://doi.org/10.1016/j.csr.2005.09.008.

Taniuchi, Y., T. Watanabe, T. Azumaya, S. Takagi, H. Kasai, T. Nakanowatari, T. Ohnishi, S. Kakehi, and H. Kuroda. 2023. "Drastic Changes in a Lower-Trophic-Level Ecosystem Attributed to Unprecedented Harmful Algal Outbreaks in 2021 on the Pacific Shelf off Southeast Hokkaido, Japan." *Continental Shelf Research* 267:105114. https://doi.org/10.1016/j.csr.2023.105114.

Terauchi, G., R. Tsujimoto, J. Ishizaka, and H. Nakata. 2014. "Preliminary Assessment of Eutrophication by Remotely Sensed Chlorophyll-A in Toyama Bay, the Sea of Japan." *Journal of Oceanography* 70 (2): 175–184. https://doi.org/10.1007/s10872-014-0222-z.

Toratani, M., K. Ogata, and H. Fukushima. 2021. "Atmospheric Correction Algorithm for Ocean Color Version 3 Oct. 28 2021, SGLI Algorithm Theoretical Basis Document." *JAXA EORC GCOM-C* homepage Accessed December 21, 2024. https://suzaku.eorc.jaxa.jp/GCOM_C/data/ATBD/ver3/V3ATBD_O2AB_NWLR_toratani.pdf.

Wang, Y., D. Liu, Y. Wang, Z. Gao, and J. K. Keesing. 2019. "Evaluation of Standard and Regional Satellite Chlorophyll-A Algorithms for Moderate-Resolution Imaging Spectroradiometer (MODIS) in the Bohai and Yellow Seas, China: A Comparison of Chlorophyll-A Magnitude and Seasonality." *International Journal of Remote Sensing* 40 (13): 4980–4995. https://doi.org/10.1080/01431161.2019.1577579.

Ward, J. H. 1963. "Hierarchical Grouping to Optimize an Objective Function." *Journal of the American Statistical Association* 58 (301): 236–244. https://doi.org/10.1080/01621459.1963.10500845.

Yamaguchi, H., J. Ishizaka, E. Siswanto, Y. B. Son, S. Yoo, and Y. Kiyomoto. 2013. "Seasonal and Spring Interannual Variations in Satellite-Observed Chlorophyll-A in the Yellow and East China Seas: New Datasets with Reduced Interference from High Concentration of Resuspended Sediment." *Continental Shelf Research* 59:1–9. https://doi.org/10.1016/j.csr.2013.03.009.

Yano, K., Y. Takayama, S. Shimode, M. Toratani, H. Murakami, and V. S. Kuwahara. 2024. "Observation of a Coccolithophore *Gephyrocapsa Oceanica* Bloom in the Temperate Coastal Waters of Sagami Bay." *Japan, Plankton and Benthos Research* 19 (1): 37–50. https://doi.org/10.3800/pbr.19.37.

Yunus, A. P., J. Dou, and N. Sravanthi. 2015. "Remote Sensing of Chlorophyll-A as a Measure of Red Tide in Tokyo Bay Using Hotspot Analysis." *Remote Sensing Applications: Society & Environment* 2:11–25. https://doi.org/10.1016/j.rsase.2015.09.002.